Progress In Electromagnetics Research, PIER 82, 167–188, 2008

AN ALTERNATIVE SOLUTION FOR THE REFLECTOR SURFACE RETRIEVAL PROBLEM

P. Bolli

Osservatorio Astronomico di Cagliari
Istituto Nazionale Astrofisica
Loc. Poggio dei Pini, 09012 Capoterra, Italy

G. Mazzarella, G. Montisci, and G. Serra

Dipartimento di Ingegneria Elettrica ed Elettronica
Univ. di Cagliari
Piazza D'Armi, 09123 Cagliari, Italy

Abstract—The retrieval of the surface profile of a reflector antenna is an important task, mainly for radio-astronomical applications. The microwave holography retrieves the reflector profile starting from a set of measured far-field data. The main step of this technique is the computation of the induced currents on the reflector surface. This requires the solution of a linear inverse problem which is strongly ill-conditioned. We propose a new technique, based on the Singular Value Decomposition, for the solution of this linear inversion problem. This technique supplies a flexible regularization scheme, able to take into account also the noise level of the data. The proposed procedure has been tested on a number of different cases, with field data generated by a commercial software.

1. INTRODUCTION

The performances of reflector antennas strongly depend on the accuracy of their surface. Therefore, the detection of the position and amount of the surface distortions is a key step in the reflector antenna test. Environmental causes, mechanical deformations due to the antenna positioning, and the changing gravitational loads when the elevation pointing direction of the antenna is modified, can degrade the surface accuracy and, as a consequence, the antenna efficiency. Therefore, the reflector surface must be periodically checked in order

to preserve the antenna performances. This is even more important for radio-astronomical reflector antennas [1–8]. Actually, some reflector antennas of recent construction have been provided with active surfaces (see e.g., the Noto Radiotelescope in Italy) to compensate for the deformations. As a consequence, the panels displacements must be evaluated and corrected by using an effective and accurate procedure.

Many different techniques have been proposed for the reflector surface measurements. These techniques can be divided into direct and inverse measurement methods. The former ones survey the reflector surface by using mechanical and/or optical measurement systems [9, 10]. The output of these technique gives the actual shape of the main reflector. On the other side, the inverse methods, based on microwave holographic measurement, examine the entire optics chain. They obtain the current induced on the reflector surface, and then the information about the surface misalignments, by using the antenna far-field pattern which is measured by pointing the reflector towards a satellite or a radio source [11]. The amplitude and phase of the far-field can be measured by using a second antenna to obtain a stable phase reference [11]. As an alternative, only the amplitude of the far-field can be used as input data [12–14]. Both types of far-field measurements allow to create an accurate map of the reflector surface. Of course, they need a high signal-to-noise ratio (SNR). This is particularly true for the phase retrieval methods [12–14], which require about the square SNR of that needed when the phase can be directly measured.

In this paper we focus our attention on the use of microwave holography for the computation of the induced current on the reflector surface, by using both amplitude and phase information of the far-field. This task requires the solution of an inverse problem, which is strongly ill-conditioned. Moreover, only a limited amount of information on the antenna pattern is available. As a consequence, the solution must be sought by using some regularization procedure.

Up to now, this problem has been solved by using an extrapolation procedure, based on a simple Fourier transform [11] inversion. This is computationally efficient, but is limited to the paraxial case. As required by the FFT algorithm, the far-field measurements must be taken at the Nyquist rate and the current sampling rate is dictated by the well-known FFT rule. This choice assures an implicit regularization of the problem [15] but the amount of regularization is independent from the noise level.

Aim of this paper is to introduce and investigate a new solution technique for this linear inversion problem based on the Singular Value Decomposition (SVD) [16]. The main advantages of this approach are: i) it is based on the exact relation between field and current and does

not require the paraxial approximation leading to the FFT inversion approach. As a consequence, it can also be implemented starting from different set of data, while FFT requires far-field paraxial data;
ii) it supplies a flexible regularization scheme, able to take into account the noise level of the data and tie it to the actual resolution (i.e., the amount of independent information);
iii) no constraint on the measurement and reconstruction points and, consequently, the separation of the actual resolution of the solution from its *graphical* resolution.

In order to assess the new holographic technique presented in this paper, a number of surface distortions of arbitrary amount and position have been considered on a test reflector. The far-field data have been obtained by using a commercial software for the analysis of general reflector antennas (GRASP 9 by TICRA).

2. PROBLEM FRAMEWORK

As it is well-known [17], the relationship between the radiated far-field $\underline{E}(r,\theta,\phi)$ and the current $\underline{J}(\underline{r}_0)$ on the reflector surface is

$$\underline{E}(r,\theta,\phi) = -j\beta\xi\frac{e^{-j\beta r}}{4\pi r}\underline{F}(\theta,\phi) \tag{1}$$

$$\underline{F}(\theta,\phi) = [\underline{\underline{I}} - \underline{i}_r\underline{i}_r]\cdot\iint_S \underline{J}(\underline{r}_0)e^{j\beta\underline{i}_r\cdot\underline{r}_0}ds \tag{2}$$

wherein $\beta = 2\pi/\lambda$, λ is the free-space wavelength and $\xi = 120\pi$ is the free-space impedance. Equation (2) gives the radiation pattern of the reflector antenna; $\underline{\underline{I}}$ is the identity matrix, $\underline{i}_r$ is the unit vector that points toward the direction (θ,ϕ), S is the surface of the parabolic reflector (with diameter D and focal length f) and $\underline{r}_0$ is the vector that points on the reflector surface element ds (see Fig. 1(a)).

We assume that the reflector antenna is illuminated by a feed, located at the focal point (O in Fig. 1(a)), with an ideal linear polarization. Since the reflector is axis-symmetric, we choose the x-axis along the E-plane of the feed. Let be $\underline{H}^i$ the incident magnetic field generated by the feed. The induced electric current $\underline{J}(\underline{r}_0)$ on the reflector depends on $\underline{H}^i$. The standard approximation to evaluate $\underline{J}(\underline{r}_0)$ is the use of the physical optics (PO) currents $\underline{J}^{(PO)}(\underline{r}_0) = 2\underline{i}_n \times \underline{H}^i(\underline{r}_0)$ [17], wherein $\underline{i}_n$ is the normal to the reflector surface.

Letting the PO currents $\underline{J}^{(PO)}(\underline{r}_0) = 2H^i\underline{i}_j$, the sought for induced current direction is

$$\underline{i}_j = \frac{\underline{i}_n \times \underline{i}_H}{|\underline{i}_n \times \underline{i}_H|} \tag{3}$$

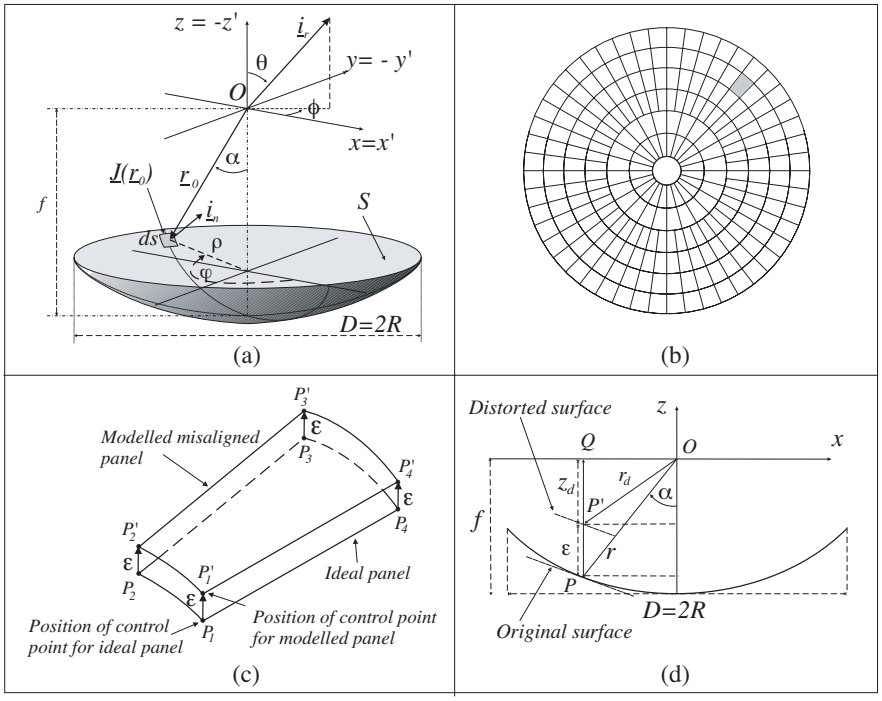

Figure 1. (a) Reflector Geometry; (b) front view of the parabolic reflector with subdivision into panels; the panel under test is highlighted in grey; (c) GRASP modelization of a panel; (d) description of the surface distortion.

where $\underline{i}_H$ is the direction of the incident magnetic $\underline{H}^i$ field.

Letting $\alpha(\rho) = 2\arctan[\rho/(2f)]$ the angle measured from the feed boresight (see Fig. 1(a)), it follows that

$$\underline{i}_H = \frac{-\sin^2\alpha\sin\varphi\cos\varphi\underline{i}_x + (1-\sin^2\alpha\sin\varphi)\underline{i}_y - \sin\alpha\cos\alpha\sin\varphi\underline{i}_z}{|-\sin^2\alpha\sin\varphi\cos\varphi\underline{i}_x + (1-\sin^2\alpha\sin\varphi)\underline{i}_y - \sin\alpha\cos\alpha\sin\varphi\underline{i}_z|} \tag{4}$$

and the unit normal $\underline{i}_n$ to the reflector surface is given by

$$\underline{i}_n = \frac{-\dfrac{\partial g}{\partial x'}\underline{i}_x - \dfrac{\partial g}{\partial y'}\underline{i}_y + \underline{i}_z}{\left|-\dfrac{\partial g}{\partial x'}\underline{i}_x - \dfrac{\partial g}{\partial y'}\underline{i}_y + \underline{i}_z\right|} \tag{5}$$

wherein $z' = g(x', y')$ describes the surface of the parabolic reflector.

The integral (2), can be written in terms of the aperture coordinates (ρ, φ) $(z' = -z,\ x' = x = \rho\sin\varphi,\ y' = -y = \rho\cos\varphi)$ by using the surface Jacobian transformation [17]:

$$\underline{F}(\theta,\phi) = [\underline{\underline{I}} - \underline{i}_r\underline{i}_r] \cdot \iint_{S'} \underline{J}(\rho,\varphi) e^{j\beta \underline{i}_r \cdot \underline{r}_0} J_s \rho d\rho d\varphi \tag{6}$$

wherein the Jacobian J_s is given by

$$J_s = \left[\left(\frac{\partial g(x',y')}{\partial x'} \right)^2 + \left(\frac{\partial g(x',y')}{\partial y'} \right)^2 + 1 \right]^{\frac{1}{2}} \tag{7}$$

The new integration domain S' in (6) is the projection of the reflector surface S on the aperture plane, and therefore is defined in the following range: $\rho \in [R_B, R]$, $\varphi \in [0, 2\pi]$, wherein R_B and R are, respectively, the blocking and external radii of the reflector.

Let now define an equivalent current $\underline{\widetilde{J}}$ such that:

$$\underline{\widetilde{J}} = \underline{J}(\rho,\varphi) J_s. \tag{8}$$

This equivalent current has a direction $\underline{i}_j$ given by (3) and will be expressed in the following as $\underline{\widetilde{J}} = \widetilde{J}\underline{i}_j$, where $\widetilde{J}$ is the unknown current to be retrieved by the far-field measurement data. Replacing $\underline{i}_r$ and $\underline{r}_0$ by their spherical components we can finally write:

$$\underline{F}(\theta,\phi) = [\underline{\underline{I}} - \underline{i}_r\underline{i}_r] \cdot \underline{i}_j \int_{R_B}^{R} \int_0^{2\pi} \widetilde{J} e^{j\beta(z' \cos\theta + \rho \sin\theta cos(\varphi - \phi))} \rho d\rho d\varphi \tag{9}$$

where $z'(\rho) = [\rho^2/(4f)] - f$ is the reflector nominal profile.

Now, since our attention is aimed at the reflector profile, i.e., at a scalar quantity, only one component of the induced current is sufficient to obtain the required information on the reflector surface. As a consequence, only one component of the far-field can be considered, and we choose the field co-polar component

$$F_c(\theta,\phi) = \underline{i}_c \cdot [\underline{\underline{I}} - \underline{i}_r\underline{i}_r] \cdot \underline{i}_j \int_{R_B}^{R} \int_0^{2\pi} \widetilde{J} e^{j\beta(z' \cos\theta + \rho \sin\theta cos(\varphi - \phi))} \rho d\rho d\varphi \tag{10}$$

because it allows for the best SNR on the data. In (10) the vector

$$\underline{i}_c = [1 - \cos^2\phi(1 - \cos\theta)]\ \underline{i}_x - (1 - \cos\theta)\sin\phi\cos\phi\ \underline{i}_y - \sin\theta\cos\phi\ \underline{i}_z \tag{11}$$

is the field co-polar component direction (Ludwig's third definition [18]), assuming that the radiated electric field is predominantly

x-polarized. Note that for large and focusing reflectors, as radio-astronomical ones, we can assume $\theta \ll 1$ (radians) ($\cos\theta \cong 1$ and $\sin\theta \cong 0$), and find an approximate expression for (11)

$$\underline{i}_c \cong \underline{i}_x. \tag{12}$$

It is worth noting that, contrarily to the FFT inversion [11], no paraxial approximation has been made in the phase terms of (10). In fact, the assumption $\theta \ll 1$, only results in the approximation of the amplitude and direction of the co-polar field component, as apparent from (12).

Equation (10) is a linear Fredholm integral equation of the first kind [16], where $\widetilde{J}(\rho,\varphi)$ is the unknown and $F_c(\theta,\phi)$ the known term. Its inversion is a severely ill-posed problem because of its very smooth kernel and the limited integration domain S' [16]. It follows that (10) cannot be directly inverted, but it is necessary to apply a regularization procedure, which generally needs also a different solution definition, in view of the fact that the measured data $F_c(\theta,\phi)$ will include an unavoidable noise. Moreover, it must be pointed out that the far-field pattern measurements are limited to a discrete number of points in the region of the antenna main lobe and first few side lobes. Therefore, the problem must be analyzed as a discrete data inverse problem [16]. Let (θ_p,ϕ_p) be the set of field measurement points (with $p = 1,\ldots,M$) and L_p the functional which supplies $F_c(\theta_p,\phi_p)$. If the f_p are the measured values, then:

$$f_p = L_p[\widetilde{J}] + n_p = f_p^t + n_p \tag{13}$$

where f_p^t is the field's "ideal" value (i.e., without noise) and n_p is the noise on the pth measure. In order to solve (13), the unknown current must be discretized too, by choosing a suitable set of basis function $I_q(\rho,\varphi)$, $q = 1,\ldots,N$. Therefore, the unknown current can be expressed as $\widetilde{J} = \sum_{q=1}^{N} J_q I_q(\rho,\varphi)$ and (13) can be rewritten as

$$f_p = \sum_{q=1}^{N} J_q L_p[I_q(\rho,\varphi)] + n_p. \tag{14}$$

If the functional L_p is not directly invertible, as in (10), the problem must be formulated in the least-squares sense. Defining the numerical vector $\underline{f} \in C^{M\times 1}$, having components f_p, and the matrix $\underline{\underline{L}}$ associated with the functional L_p, we must seek for a solution $\underline{\widetilde{J}}_{LS}$ (having component J_q) that minimizes the residual 2-norm

$$\min_{\underline{\widetilde{J}}\in C^{N\times 1}} \|\underline{\underline{L}}\cdot\underline{\widetilde{J}} - \underline{f}\|_2^2. \tag{15}$$

This solution is usually termed "least-squares solution" [16], and it depends linearly on the data $\underline{f}$, so that we can write

$$\underline{\widetilde{J}}_{LS} = \underline{\underline{L}}^{\dagger} \cdot \underline{f} \tag{16}$$

wherein $\underline{\underline{L}}^{\dagger}$ is the so-called generalized inverse of the matrix $\underline{\underline{L}}$ [16]. The main point is that, even though this discrete data problem is well-posed, it turns out to be heavily ill-conditioned [16], because (10) is ill-posed.

3. SOLUTION APPROACH

The approach described in this paper consists in finding the unknown current $\widetilde{J}$ on the reflector surface by using a formulation like (16). Therefore, $\widetilde{J}$ is discretized according to the required *graphical* resolution and the least-squares solution is regularized by using the SVD.

The SVD approach applied to the calculation of a large linear system, as that deriving from the application of (16) to a large reflector antenna, is computationally heavy. However, this problem can be overcome by using some features of radio-astronomical reflectors. In fact, they are axis-symmetric, so that both the surface current and the radiation pattern are better represented as Fourier Series. Obviously, for numerical computation, it is necessary to truncate the series to a finite number of terms with suitable upper limits. These limits can be determined by exploiting the fact that the radiation pattern is a quasi-band-limited function [19]. This property suggests that the number of the retained series terms can be obtained by the spatial bandwidth of the scattered field, as widely discussed in [19]. For a large scattering system, the effective bandwidth of the scattered field, measured on a circular domain, can be identified as

$$w = \frac{2P+1}{2\sin\theta_{max}} = \chi\beta R \tag{17}$$

wherein R is the radius of the sphere which includes the scatterer (we assume it equal to the radius of the reflector); χ is an excess bandwidth factor and has to be chosen slightly larger than unity to ensure a negligible representation error [19]; θ_{max} is the maximum value of the θ angle of the measured circular domain and $2P+1$ is the number of the Fourier harmonics. Solving (17) with respect to P, it follows that the number of harmonics for each side of the series is

$$P \cong \chi\beta R\sin\theta_{max}. \tag{18}$$

Therefore, letting $C_i(\rho)$ the ith harmonic of the current and $t_i(\theta)$ the ith harmonic of the field, the truncated Fourier series representation for the current and the radiation pattern is

$$\widetilde{J}(\rho,\varphi) = \sum_{i=-P}^{P} C_i(\rho) e^{j(i\varphi)}, \;\; F_c(\theta,\phi) = \sum_{i=-P}^{P} t_i(\theta) e^{j(i\phi)} \tag{19}$$

wherein each harmonic $t_i(\theta)$ can be calculated as

$$2\pi t_i(\theta) = \int_0^{2\pi} F_c(\theta,\phi) e^{-j(i\phi)} d\phi. \tag{20}$$

Now, carrying out the scalar products in (10), substituting the expressions (19) in (10), and using the approximated expression (12), after calculating the integrals with respect to the variables φ and ϕ, we get a set of $2P+1$ equations, one for each harmonic

$$\begin{aligned} t_i(\theta) \cong (j)^i 2\pi \int_{R_B}^{R} \left[2\cos\left(\frac{\alpha}{2}\right) - \sin\alpha \sin\left(\frac{\alpha}{2}\right) \right] Q_i(\rho,\theta) C_i(\rho) \rho d\rho \\ + (j)^i \frac{\pi}{4} \int_{R_B}^{R} \sin\alpha \sin\left(\frac{\alpha}{2}\right) Q_i(\rho,\theta) [C_{i-2} + C_{i+2}](\rho) \rho d\rho \end{aligned} \tag{21}$$

with $Q_i(\rho,\theta) = J_i(\beta\rho\sin\theta) e^{j\beta z(\rho)\cos\theta}$, wherein J_i is the Bessel function of the first kind. As it is apparent from (21), the series representation of the current involves a coupling between different harmonics, so that the ith harmonic of the field $t_i(\theta)$ is weakly coupled with the *(i-2)*th and *(i+2)*th harmonics of the current (C_{i-2} and C_{i+2}). Actually, the amplitude of the coupling terms, i.e., $\sin(\alpha)\sin(\alpha/2)$, increases with the angle α under which the feed subtends the reflector and so decreases when the focal diameter ratio (f/D) increases. However, we found that the magnitude of the coupling terms is small enough even for the small f/D values typical for radio-astronomical antennas. Therefore, they are neglected and we are left with a new set of $2P+1$ equations which are decoupled:

$$t_i(\theta) \cong (j)^i 4\pi \int_{R_B}^{R} \cos\left(\frac{\alpha}{2}\right) Q_i(\rho,\theta) C_i(\rho) \rho d\rho. \tag{22}$$

4. REGULARIZED SOLUTION

The Fredholm equation (22) can be transformed in a linear system by representing the coefficient of the ith Fourier harmonic $C_i(\rho)$ in terms of a set of piecewise-constant basis functions $\hat{I}_q(\rho)$, $q =$

$1, \ldots, N$. Therefore, we subdivide the integration domain of (22) into N subdomains such that:

$$\Delta\rho = \frac{R - R_B}{N}. \tag{23}$$

Then, we sample both sides of (22) at the measurement points. This latter is not a direct task, since $F_c(\theta, \varphi)$ (and then $t_i(\theta)$) requires the measurement points to be located on concentric circles (antenna framework), while typical measured data are available in azimuth-elevation coordinates (terrestrial framework). Therefore, a data transformation is required, and can be performed in two steps:
i) the measured data are transformed from the terrestrial framework (a regular lattice in azimuth-elevation) to the antenna framework, which can be considered a regular lattice in (u, v) for small θ angles (wherein $u = \sin\theta\cos\phi$, $v = \sin\theta\sin\phi$);
ii) the new data in the antenna framework are interpolated in a set of points placed on concentric circles with equi-spaced values $\theta_p = p\Delta\theta$, with $p = 1, \ldots, M$ and $\Delta\theta = \theta_{max}/M$. This interpolation is performed by using band-limited self-truncating functions [20, 21] and, for each values of θ_p, the number of interpolating points n_ϕ, with respect to the ϕ coordinate, is determined by the constraint on the limited spatial band of the reflector field [19], i.e., $n_\phi(\theta_p) = \chi\beta R\sin\theta_p$. Therefore, the sample spacing along each circle θ_p is $\Delta\phi_p = 2\pi/[2n_\phi(\theta_p) + 1]$.

The number of unknowns involved in the least-squares problems is determined by the choice of N (23). Nevertheless, for each harmonic we have a different linear system, with different matrix and data vector. More precisely, a given circular ring, at a distance R_0 from the reflector axis (i.e., all the reflector point with $\rho \cong R_0$) produces, in the measurements region, only field harmonics up to $\hat{P}(R_0) = \chi\beta R_0\sin\theta_{max}$ (see Equation (18)). Therefore, its current must be retrieved by using only the harmonics in the range $[-\hat{P}(R_0), \hat{P}(R_0)]$. As a consequence, for the ith harmonic, only $\widetilde{N}_i \leq N$ unknowns are involved in the ith linear system.

Furthermore, for each measurement point θ_p, the limited spatial bandwidth of the scattered field is $(2\widetilde{P} + 1)/2\sin\theta_p = \chi\beta R$. This means that the maximum index of the Fourier harmonics $\widetilde{P}(\theta_p)$ is given by $\widetilde{P}(\theta_p) = \chi\beta R\sin\theta_p$. As a consequence, the number of equations $\widetilde{M}_i \leq M$, in the linear system for the ith harmonic of the current, is a decreasing function of i.

Then, let A^i be the vector whose components are the coefficients

of the expansion of the harmonic $C_i(\rho)$ in terms of the set $\{\hat{I}_q(\rho)\}$

$$C_i(\rho) = \sum_{q=N-\widetilde{N}_i+1}^{N} A_q^{(i)} \hat{I}_q(\rho) \tag{24}$$

and T^i the vector with components $\underline{t}^i(\theta_p)$ with $p = M - \widetilde{M}_i + 1, \ldots, M$. Since the solution of each ith linear system can be found in the same way, and independently from the others, we discuss here the solution technique for the general form of such systems

$$\underline{\underline{L}} \cdot \underline{A} = \underline{T} \tag{25}$$

wherein $\underline{\underline{L}} \in C^{\widetilde{M}\times\widetilde{N}}$, $\underline{A} \in C^{\widetilde{N}\times 1}$, $\underline{T} \in C^{\widetilde{M}\times 1}$.

Equation (25) can be solved in the least-squares sense [16], by using a regularization procedure based on the SVD of the matrix $\underline{\underline{L}}$:

$$\underline{\underline{L}} = \underline{\underline{U}} \cdot \underline{\underline{\Sigma}} \cdot \underline{\underline{V}}^H \tag{26}$$

wherein $\underline{\underline{U}}$, $\underline{\underline{V}} \in C^{\widetilde{M}\times\widetilde{N}}$ are matrices with orthonormal columns, the apex H denotes the Hermitian matrix of $\underline{\underline{V}}$, and $\underline{\underline{\Sigma}} = diag(\sigma_1, \ldots, \sigma_{\widetilde{N}}) \in C^{\widetilde{N}\times\widetilde{N}}$ is a diagonal matrix. The diagonal elements, the so called singular values of matrix $\underline{\underline{L}}$, are non-negative and appear in non-increasing order such as $\sigma_1 \geq \sigma_2 \geq \ldots \sigma_{\widetilde{N}}$. Moreover, the ratio between the highest singular value σ_1 and the lowest non-zero one σ_r, is the condition number of the matrix $\underline{\underline{L}}$, i.e., $cond(\underline{\underline{L}}) = \frac{\sigma_1}{\sigma_r}$ [16].

Roughly speaking, the condition number of $\underline{\underline{L}}$ is the ratio between the relative errors in the solution and in the data, and it is therefore a measure of the robustness of the solution. Actually, all the diagonal elements of the matrix $\underline{\underline{\Sigma}}$ are different from zero only when $\widetilde{M} \geq \widetilde{N} = r$, where r is the rank [16] of matrix $\underline{\underline{L}}$. On the other hand, if $\widetilde{N} > \widetilde{M}$, (25) is an under-determined linear system and $r \leq \widetilde{N}$. Therefore, if $\widetilde{N} \leq \widetilde{M}$ the diagonal matrix $\underline{\underline{\Sigma}}$ is $diag(\sigma_1, \ldots, \sigma_r) \in C^{\widetilde{N}\times\widetilde{N}}$, whereas if $\widetilde{N} > \widetilde{M}$ the diagonal matrix $\underline{\underline{\Sigma}}$ can be more correctly written as $diag(\sigma_1, \ldots, \sigma_r, 0, \ldots, 0) \in C^{\widetilde{N}\times\widetilde{N}}$. In the following discussion, for the sake of simplicity, we assume $\widetilde{N} < \widetilde{M}$. Nevertheless, the results of the regularization procedure is exactly the same if $\widetilde{N} \geq \widetilde{M}$, provided that we use the diagonal matrix with zeroes in the positions $r+1, \ldots, \widetilde{N}$.

Once computed the SVD of the matrix $\underline{\underline{L}}$, for each ith harmonic,

we seek for the least-squares solution $\underline{A}_{LS}$ such that:

$$\min_{\underline{A}\in\ C^{\widetilde{N}\times 1}} \left\| \underline{\underline{L}}\ \underline{A} - \underline{T} \right\|_2^2 = \min_{\underline{A}\in\ C^{\widetilde{N}\times 1}} \left\| \underline{\underline{U}}\ \underline{\underline{\Sigma}}\ \underline{\underline{V}}^H \underline{A} - \underline{T} \right\|_2^2. \tag{27}$$

After left-multipling (27) by $\underline{\underline{U}}^H$, we can put $\underline{x} = \underline{\underline{V}}^H \underline{A}$ and $\underline{z} = \underline{\underline{U}}^H \underline{T}$. Then, (27) becomes

$$\min_{\underline{x}\in\ C^{\widetilde{N}\times 1}} \left\| \underline{\underline{\Sigma}}\ \underline{x} - \underline{z} \right\|_2^2 = \min_{\underline{x}\in\ C^{\widetilde{N}\times 1}} \sum_{k=1}^{r} [\sigma_k x_k - z_k]^2. \tag{28}$$

Equation (28) is minimized with respect to the unknowns x_k when $x_k = z_k/\sigma_k$. Therefore, the vector solution set of (28) is

$$\underline{x} = \left(\frac{\underline{u}_1^H \underline{T}}{\sigma_1}, \ldots, \frac{\underline{u}_r^H \underline{T}}{\sigma_r} \right)^T \tag{29}$$

wherein $\underline{u}_k$ are the columns of the matrix $\underline{\underline{U}}$ and the apex T denotes the transpose operator. Finally, the minimum *2*-norm solution (or least-squares solution) of (28) is

$$\underline{A}_{LS} = \underline{\underline{V}} \cdot \left(\frac{\underline{u}_1^H \underline{T}}{\sigma_1}, \ldots, \frac{\underline{u}_r^H \underline{T}}{\sigma_r} \right)^T = \underline{\underline{L}}^{\dagger} \cdot \underline{T} \tag{30}$$

wherein $\underline{\underline{L}}^{\dagger} = \underline{\underline{V}} \cdot diag(1/\sigma_1, \ldots, 1/\sigma_r) \cdot \underline{\underline{U}}^H$ is the generalized inverse matrix of $\underline{\underline{L}}$.

If the matrix $\underline{\underline{L}}$ were well-conditioned (i.e., with a small condition number), the stability of the solution of the linear system (25) would be ensured. Nevertheless the ill-posedness of (22) makes the matrix $\underline{\underline{L}}$ ill-conditioned. To better clarify this concept, we can express the solution $\underline{A}_{LS}$ in terms of components

$$\underline{A}_{LS} = \underline{\underline{L}}^{\dagger} \cdot \underline{T} = \sum_{k=1}^{r} \frac{\underline{u}_k^H \underline{T}}{\sigma_k}\ \underline{v}_k \tag{31}$$

wherein $\underline{v}_k$ are the columns of the matrix $\underline{\underline{V}}$. The ill-conditioning of the matrix $\underline{\underline{L}}$ is usually due to several "small" (compared to the norm of σ_1) but non-zero singular values. As a result, $\underline{A}_{LS}$ becomes unstable, since the smallest σ_k increases the condition number and then amplifies the noise in the solution. In other words, the ratio $|\underline{u}_k^H \underline{T}|/\sigma_k$ in (31) increases very quickly with k and, in presence of noise on the known term $\underline{T}$, the solution instability becomes more

evident (see Fig. 2). As shown in Fig. 2(b) for a typical case, this result is critical for the least-squares solution of the higher harmonics. Actually, for example, in presence of noise, the contribution of the harmonic ♯10 is comparable to that of the harmonic ♯0 for high values of k, whereas the two contributions are still well apart for low values of k as well as in the noiseless case.

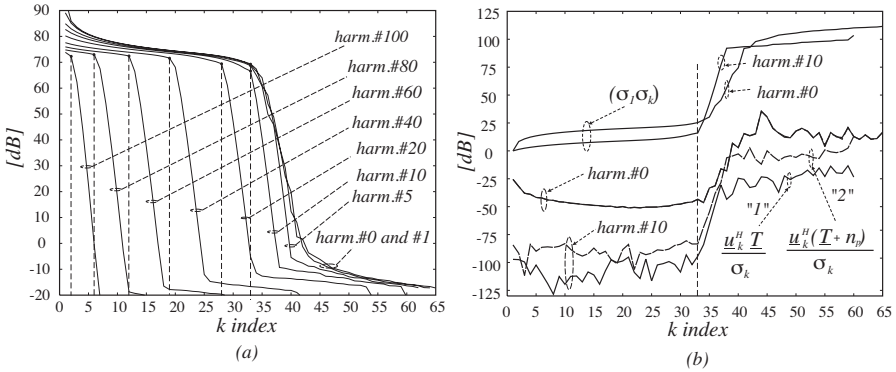

Figure 2. (a) Typical step like behaviour of the singular values for a number of selected harmonics; (b) typical behaviour of the least-squares solution, for the harmonics ♯0 and ♯10, by using the SVD approach applied to a test distortion. The curves "1" and "2" show respectively the coefficients of the solution without noise and with a Signal-Noise Ratio equal to 63 dB (zero-mean Gaussian noise calculated with the respect to the maximum of the signal) for the harmonic ♯10. The coefficient of the solution for the harmonic ♯0 are virtually unaffected by the noise effect for a SNR of 63 dB.

The ill-conditioned system can be regularized by replacing the matrix $\underline{\underline{L}}$ by a new matrix $\underline{\underline{L}}_G$, defined as

$$\underline{\underline{L}}_G = \underline{\underline{U}} \cdot diag(\sigma_1, \ldots, \sigma_G, 0, \ldots, 0) \cdot \underline{\underline{V}}^H \tag{32}$$

wherein we replace the small non-zero singular values $\sigma_{G+1}, \ldots, \sigma_r$ with exact zeros [16]. Therefore, when $\underline{\underline{L}}$ is replaced by $\underline{\underline{L}}_G$, we obtain a regularized solution

$$\underline{A}_{LS} = \underline{\underline{L}}_G^{\dagger} \cdot \underline{T} = \sum_{k=1}^{G} \frac{\underline{u}_k^H \underline{T}}{\sigma_k} \, \underline{v}_k \tag{33}$$

wherein $\underline{\underline{L}}_G^{\dagger} = \underline{\underline{V}} \cdot diag(1/\sigma_1, \ldots, 1/\sigma_G, 0, \ldots, 0) \cdot \underline{\underline{U}}^H$ is the generalized inverse matrix of $\underline{\underline{L}}_G$. In practise, since the ratio $|\underline{u}_k^H \underline{T}|/\sigma_k$ has a step-like behaviour for increasing values of the index k (see Fig. 2(b)), we

choose the G value just before the knee of the curve representing the singular value behaviour [16], in order that the condition number of the solution (i.e., $N_c = \sigma_1/\sigma_G$) remains bounded.

Of course, the choice of G must be repeated for each harmonic, since the matrix $\underline{\underline{L}}$ is different. In Fig. 2(a), we show the behaviour of the singular values in a typical case for a number of selected harmonics of the recovered surface current.

Once the least-squares solution $\underline{A}_{LS}^{(i)}$ is computed, for each ith linear system, we can find the currents on the reflector as the sum of Fourier harmonics:

$$J_{LS}(\rho,\varphi) = \sum_{i=-P}^{P} C_i(\rho)\exp[j(i\varphi)] = \sum_{i=-P}^{P} \sum_{q=N-\widetilde{N}_i+1}^{N} A_q^{(i)} \hat{I}_q(\rho)\exp[j(i\varphi)] \tag{34}$$

where the discretization of radial coordinate ρ depends on the sampling points of the $J_{LS}(\rho,\varphi)$, whereas the angular coordinate φ is suitably discretized according to the required graphical resolution.

The currents induced on the reflector surface (34) are related to the surface profile, and the comparison between the calculated profile and the nominal profile allows us to find the distortions of the reflector surface. In order to extract the surface profile information from (34), we assume that the phase center of the feed is placed at the focal point and that the surface distortion is described by the function $\varepsilon(x,y)$ in the z direction, as shown in Fig. 1(d). After simple geometric considerations the surface distortion is obtained as

$$\varepsilon(x,y) = \frac{\lambda}{2\pi(1+\cos\alpha)}\Delta\delta. \tag{35}$$

wherein $\Delta\delta = phase(J_{ref}) - phase(J_{LS})$ is the difference between the phase of the reference current (induced on a reflector surface without deformations) and the phase of the recovered current. Both phases need to be unwrapped and a simple 2D unwrapping procedure has been used [22].

5. RESULTS

In order to assess the proposed technique, many different tests have been performed on a reflector with the same geometrical configuration of the Noto (Italy) antenna. The reflector diameter is 32 m, the sub-reflector diameter is 3.2 m and the focal length-diameter ratio is 0.32. For the sake of simplicity, in our tests, we suppose to neglect the blockage effects due to the sub-reflector and the quadripod. Since the

surface distortions are detected as the difference of two phases (35), these effects could be easily considered in the procedure just including the quadripod and the sub-reflector both in the choice of reference current and in the computation of recovered one.

The reflector far-field has been simulated with GRASP, at the operating frequency of 11.42 GHz, on a grid of 65×65 measurement points in the terrestrial framework (observation window between $-1.25°$ and $1.25°$) and then interpolated in the antenna framework (observation window with $\theta_{max} = 1.75°$) using the self-truncating functions [20]. The reflector model, created with GRASP, subdivides the reflector surface in a number of panels (Fig. 1(b) and 1(c)), whose dimensions and possible displacements with respect to the ideal profile, can be assigned arbitrarily. In our case the number and the location of the panels have been chosen the same of the Noto antenna.

First of all, the phase of J_{ref} (i.e., the surface current in the reference case), is evaluated starting from the reference far-field, i.e., the far-field pattern generated by the nominal reflector, without any surface deformation. Then, a far-field pattern is generated starting from a surface profile with a test deformation obtained with a panel displacement in the z direction. Finally, we get the estimation of this surface deformation by applying the SVD approach, described in the previous sections, to retrieve both J_{ref} and J_{LS} and by using (35).

In order to assess our procedure, in this section we consider in detail a deformation generated by the displacement of a test panel. The location of this panel (Fig. 1(b)) is identified by the following coordinates $\rho = [11.53\,\mathrm{m}, 13.8\,\mathrm{m}]$, $\varphi = [45°, 52.5°]$.

In the GRASP modelling, each panel has up to four control points ($P1$, $P2$, $P3$ and $P4$), i.e., the position of the panel vertexes (Fig. 1(c)). For the sake of simplicity, we impose the panel misalignment by modifying only the z coordinate of each control point of the same amount ε for all the control points.

The regularization procedure requires a suitable choice of the parameter G (the maximum number of singular values) for each harmonic. According to Section 4, we choose the value $G = \widetilde{G}$, for each ith harmonic, just before the knee of the curve representing the singular values behaviour (see Fig. 2(a)). From an accurate analysis of the solution we found that this choice is the optimal one, since we found that it minimizes the RMS error (we call it RMS_U), i.e., the phase oscillations, in the zone of the reflector different from the displaced panel and this result has shown to be independent from the distortion amount. For $G < \widetilde{G}$ there is a loss of information, which, of course, becomes more significant as G becomes smaller. On the other hand, for $G > \widetilde{G}$, the numerical errors intrinsic with the procedure, give rise

to a typical, unwanted and growing, oscillating behaviour even where the surface profile is supposed to be undistorted.

Moreover, it has been observed that the harmonics requiring $\widetilde{G} = 1$ do not contribute to the solution. They only add numerical noise to the result and therefore, in the following of this section, will be always neglected. All other harmonics will be included in the solution for noiseless far-field data whereas, in the case of noisy data, only those harmonics with the components of $\underline{T}$ large enough with respect to the noise will be retained. The quantitative criterion will be described later in this section.

5.1. Results for Noiseless Far-Field Data

As a first step, a displacement of the panel highlighted in Fig. 1(b) has been recovered in the case of noiseless far-field measurements. A comparison with the results of the traditional FFT inversion has been also performed.

In Fig. 3 the gray scale map of the reflector, obtained with the SVD-based approach, with a recovered panel distortion of amount 0.2 mm ($\lambda_0/130$ at 11.42 GHz), is shown. The same distortion has been recovered with the iterative FFT-inversion proposed by Rahmat-Samii [11], showing virtually no differences in terms of resolution and amount of the recovered distortion.

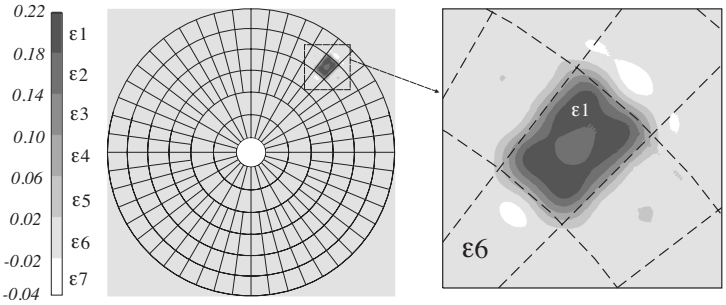

Figure 3. Gray scale map of the retrieved reflector surface for a distortion of 0.2 mm of the panel under test.

On equal graphic resolutions (0.3 m), the FFT-inversion is computationally faster (it takes about 1.5 sec on a "AMD Athlon 2500+" machine with 1 GB RAM) but with the same magnitude order of our SVD approach (about 5 sec). This difference is not critical since the time required for the far field measurement campaign is of the order of a few hours.

The actual spatial resolution in the retrieval of a surface distortion is determined by the number of singular values used in the SVD regularization procedure, which gives the degrees of freedom in the retrieval of the reflector surface current. Therefore, the spatial resolution can be evaluated by using $R_S = \sqrt{A_f/N_\nu}$, wherein A_f is the area of the projection of the reflector surface S on the aperture plane, and N_v is the total number of singular values for all the harmonics used in the procedure. In our case, for noiseless far-field data (with an excess bandwidth factor $\chi = 1.203$), we use 211 harmonics, $N_v = 3371$ and then $R_s = 0.49\,\mathrm{m}$.

5.2. Results for Noisy Far-Field Data

The regularization scheme considered up to now in this section has been also extensively checked in the more realistic case of noisy far-field data. Also in this case a comparison with the FFT inversion has been performed showing virtually the same robustness to the noise. On the other side, contrarily to the FFT-inversion, where the amount of regularization is independent from the noise level, in this paragraph we will show how our SVD approach allows to tie the noise level to the actual resolution of the recovered distortion.

The results shown in the following have been obtained from far-field data affected by a zero-mean additive complex Gaussian noise. Therefore, the noisy samples, according to the interpolation described in *ii*) of Section 4, for each $k = 1, \ldots, 2n_\phi(\theta_p) + 1$, can be written as:

$$F_c(\theta_p, \phi_k) = F_c^t(\theta_p, \phi_k) + n_R(\theta_p, \phi_k) + jn_I(\theta_p, \phi_k);\ p = 1, \ldots, M \quad (36)$$

wherein F_c^t is the field's "ideal" value, and n_R and n_I are independent Gaussian distributions with mean zero and standard deviation $\sigma = \max_{p,k}[F_c]/SNR$. The definition of σ also fixes the SNR calculated with respect to the maximum of the signal (so that the noise is significantly higher in the external part of the measurement domain).

The noise on the far-field samples "propagates" to the known term $\underline{T}^i$ of the solution system (25) for each ith harmonic, and, from (20), we can easily derive that the components of $\underline{T}^i$ can be written as

$$t_i(\theta_p) = t_i^t(\theta_p) + x_R(\theta_p) + jx_I(\theta_p),\ p = M - \widetilde{M}_i + 1, \ldots, M \quad (37)$$

wherein x_R and x_I are Gaussian distributions with mean zero and standard deviation $\sigma_p = \sigma/\sqrt{2n_\phi(\theta_p) + 1}$. Therefore, the standard deviation σ_p has a different value for each component of the known term $\underline{T}^i$. This means that the noise on the far-field data affects in a different way each component of the known term for each harmonic.

In order to filter the noise effect we choose to neglect, in the least-squares solution, the contribution of the harmonics such that a certain percentage of the components of the known term $\underline{T}^i$ are too noisy, i.e., when

$$\sigma_{i,p} > |t_i(\theta_p)|. \tag{38}$$

This is obtained by defining a suitable threshold for the percentage of elements of $\underline{T}^i$, fulfilling the (38), which identifies a "noisy harmonic" to be neglected.

Before defining a rule for the choice of the threshold for the "noisy harmonics", it is instructive to show an example of a retrieved reflector distortion, in the case of noisy far-field data, but using the same number of harmonics used in the noiseless case. This result is shown in Fig. 4(a) for a 0.2 mm displacement of the test panel, with a SNR of 68 dB. The noise effect varies with the amplitude of taper illumination, and it is higher where the amplitude of the current is smaller. In order to test the accuracy of the edge current reconstruction, we have used an x-polarized Hertzian dipole feed. As expected, the noise effect is concentrated in the left/right edges of the reflector.

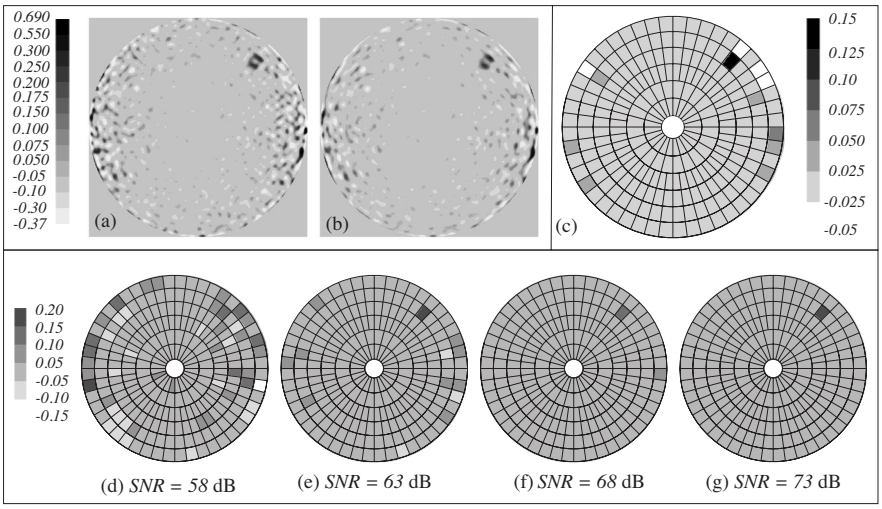

Figure 4. (a), (b), (c): gray scale map of the retrieved reflector surface for a distortion of 0.2 mm of the panel under test, $SNR = 68$ dB:(a) before noise filtering, (b) after noise filtering with, (c) all the distorted points of each panel in map (b) have been replaced by their mean value; (d), (e), (f), (g): gray scale maps of the retrieved reflector surface for a distortion of 0.2 mm of the panel under test for different values of the SNR.

In Fig. 4(a), the position of the displaced panel and the amount of the distortion are both corrupted by the noise and, in particular, by the relatively strong oscillations that rise out at the edge of the reflector and propagate towards the inner region. It is reasonable that these oscillations can be reduced by neglecting some "noisy harmonics". Therefore, the threshold that identifies these harmonics can be derived by requiring to minimize the RMS error in the undistorted reflector surface, provided that the consequent reduction of the number of harmonics does not cause too much loss of information and then, the vanishing of the deformation. Since the higher order harmonics are responsible only for the current in border region of the reflector (18), it is reasonable that the "cut" mainly concerns these harmonics.

At the end, we define s as the percentage of noisy components of $\underline{T}$ according to (38) and we neglect all the harmonics with s greater than a suitable threshold s_r. Of course, the lower is s_r, the higher is the number of neglected harmonics.

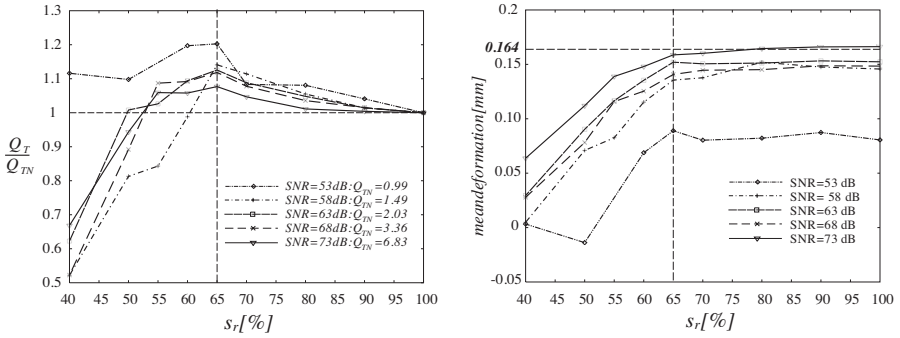

(a) (b)

Figure 5. (a) Normalized Q_T ($Q_{TN} = Q_T(s_r = 100\%)$) and (b) mean deformation of the test panel vs. s_r.

Let us define the ratio Q_T between the RMS of the displaced panel (RMS_D) and the RMS error of the rest of the reflector (RMS_U). As can be easily deduced from Fig. 5, the optimal value of s_r is between 60% and 70%. This choice ensures the maximum value of Q_T, without loosing information about the distorted panel. The choice of a $s_r < 60\%$ implies an excessive reduction of the harmonics. This allows a strong reduction in the amplitude of the unwanted oscillations, but also produces a strong loss of information. All the choices of $s_r > 70\%$ also allow an improvement with respect to the "unfiltered" results, but the noise filtering is not effective.

Of course this discussion makes sense provided that Q_T is big

enough to avoid that the distorted panel position and displacement amount are completely hidden by noise. This happens when $Q_T < 2$. In this case the choice of the threshold s_r is worthless.

In Fig. 4(b) the map of a displacement of 0.2 mm of the test panel is shown, after the noise effect has been filtered with a threshold $s_r = 65\%$. As a consequence, the number of harmonics reduces, with respect to the case of Fig. 4(a), from 211 to 93, and the number of singular values from 3371 to 2365.

Since the reflector surface is subdivided into panels, a better representation could be obtained by replacing all the distorted points belonging to each panel with their mean value. In this way we obtain the map in Fig. 4(c).

As pointed out in Section 4, the presented SVD regularization is robust with request to noise and this is the main reason for the high value of the optimal threshold s_r. In other words, this means that only highly noisy harmonics are to be neglected because a sort of noise pre-filtering has been already taken into account in the choice of G_i.

It is also worth noting that the noise filtering due to the removal of "noisy harmonics" explicitly leads to a reduction of the degrees of freedom of our least-squares problem and, as expected, to a reduction of total number of singular values and consequently of the actual resolution. In Table 1 the results for different values of the SNR are summarized and the corresponding maps are shown in Fig. 4(d)–4(g).

Table 1. Distortion of amount 0.2 mm of the panel under test for different values of the SNR. P_T is the displaced test panel. P_U ($U \neq T$) is the panel with the highest mean deformation. N_H is the number of harmonics used in the solution.

SNR [dB]	s_r %	$Mean\ in$ P_T[mm]	$Mean\ in$ P_U[mm]	Q_T	RMS_U [mm]	N_H	N_v	$Fig.$
53	–	0.089	–	$\cong 1$	0.215	–	–	Not shown
58	65	0.135	0.172	1.71	0.118	80	2119	Fig.4(d)
63	65	0.152	0.079	2.28	0.070	85	2248	Fig.4(e)
68	65	0.143	0.051	3.76	0.040	93	2365	Fig.4(f)
73	65	0.159	0.017	7.36	0.023	103	2547	Fig.4(g)
∞	-	0.164	0.002	61.2	0.0027	211	3371	Fig.3

6. CONCLUSION

The surface profile reconstruction of large reflector antennas has been faced with a new microwave holographic technique. This technique is based on the SVD and it allows to formulate and solve the problem without resorting to the usual "paraxial case" approximation. As a consequence, a wider measurement interval can be allowed. Moreover, contrarily to the FFT approach, the proposed procedure could be implemented starting from a data set different from the far-field pattern. A thorough analysis, using the well-assessed GRASP commercial software, has shown both the accuracy of the technique, and the relations between the measurement specification (e.g., the noise on the data) and the reconstruction specification (e.g., the spatial resolution).

REFERENCES

1. Bucci, O. M., A. Capozzoli, and G. D'Elia, "An effective power synthesis technique for shaped," *Progress In Electromagnetics Research*, PIER 39, 93–123, 2003.
2. Joardar, S., "Design and analysis of a low-frequency radio telescope for Jovian radio emission," *Progress In Electromagnetics Research*, PIER 72, 127–143, 2007.
3. Joardar, S. and A. B. Bhattacharya, "Simultaneous resolving of frequency separated narrow band terrestrial radio sources," *Journal of Electromagnetic Waves and Applications*, Vol. 20, 1195–1209, 2006.
4. Joardar, S. and A. B. Bhattacharya, "Algorithms for categoric analysis of interference in low frequency radio astronomy," *Journal of Electromagnetic Waves and Applications*, Vol. 21, 441–456, 2007.
5. Tian, Y., Y. H. Zhang, and Y. Fan, "The analysis of mutual coupling between paraboloid antennas," *Journal of Electromagnetic Waves and Applications*, Vol. 21, 1191–1203, 2007.
6. Joardar, S. and A. B. Bhattacharya, "A novel method for testing ultra wideband antenna-feeds on radio telescope dish antennas," *Progress In Electromagnetics Research*, PIER 81, 41–59, 2008.
7. Karimkashi, S. and J. Rashed-Mohassel, "Side lobe level reduction in symmetric dual reflector antennas using a small lens antenna," *Journal of Electromagnetic Waves and Applications*, Vol. 20, 1807–1816, 2006.

8. Karimkashi, S. and J. Rashed-Mohassel, "Blockage minimization in symmetric dual-reflector antennas for different edge taper values," *Journal of Electromagnetic Waves and Applications*, Vol. 20, 505–514, 2006.
9. Kesteven, M. J., B. F. Parsons, and D. E. Yabsley, "Antenna reflector metrology," *IEEE Trans. Antennas Propagat.*, Vol. 36, 1481–1484, 1988.
10. Subrahmanyan, R., "Photogrammetric measurement of the gravity deformation," *IEEE Trans. Antennas Propagat.*, Vol. 53, 2590–2596, 2005.
11. Rahmat-Samii, Y., "Surface diagnosis of large reflector antennas using microwave holographic metrology," *Radio Science*, Vol. 19, 1205–1217, 1984.
12. Bucci, O. M., G. D'Elia, and G. Romito, "Reflector distortions diagnosis from far-field amplitude pattern," *IEEE Trans. Antennas Propagat.*, Vol. 43, 1217–1225, 1995.
13. Capozzoli, A. and G. D'Elia, "Global optimization and antennas synthesis and diagnosis, part one," *Progress In Electromagnetics Research*, PIER 56, 195–232, 2006.
14. Capozzoli, A. and G. D'Elia, "Global optimization and antennas synthesis and diagnosis, part two," *Progress In Electromagnetics Research*, PIER 56, 233–261, 2006.
15. Papoulis, A., "A new algorithm in spectral analysis and band-limited extrapolation," *IEEE Trans. Circuits Syst.*, Vol. CAS-22, 735–742, 1975.
16. Hansen, C., *Rank-deficient and Discrete Ill-posed Problems*, SIAM, New York, 1998.
17. Balanis, C. A., *Antenna Theory, Analysis and Design*, John Wiley and Sons Inc., New York, 1997.
18. Ludwig, A. C., "The definition of cross-polarization," *IEEE Trans. Antennas Propagat.*, Vol. 21, 116–119, 1973.
19. Bucci, O. M. and G. Franceschetti, "On the spatial bandwidth of scattered fields," *IEEE Trans. Antennas Propagat.*, Vol. 35, 1445–1455, 1987.
20. Bucci, O. M. and G. Di Massa, "The truncation error in the application of sampling series to electromagnetic problems," *IEEE Trans. Antennas Propagat.*, Vol. 36, 941–946, 1988.
21. D'Agostino, F., F. Ferrara, C. Gennarelli, R. Guerriero, and G. Riccio, "An effective technique for reducing the truncation error in the near-field-far-field transformation with plane-polar scanning," *Progress In Electromagnetics Research*, PIER 73, 213–

238, 2007.

22. Cho, B. L. and Y. S. Kim, "Multilook coherence estimation using adaptive weighted window in interferometric SAR," *Journal of Electromagnetic Waves and Applications*, Vol. 21, 359–365, 2007.